Available online at www.sciencedirect.com
ScienceDirect
Journal of Nuclear Materials 363–365 (2007) 476–483
journal of nuclear materials
www.elsevier.com/locate/jnucmat

Pedestal, SOL and divertor plasma properties in DIII-D RMP ELM-suppressed discharges at ITER relevant edge collisionality

M.E. Fenstermacher [a,*], T.E. Evans [b], R.A. Moyer [c], G.D. Porter [a], J.A. Boedo [c], K.H. Burrell [b], M. Groth [a], I. Joseph [c], T.H. Osborne [b], J.G. Watkins [d]

[a] *Lawrence Livermore National Laboratory, P.O. Box 808, Livermore, CA 94550, USA*
[b] *General Atomics, P.O. Box 85608, San Diego, CA 92186-5608, USA*
[c] *University of California, San Diego, La Jolla, CA 92093, USA*
[d] *Sandia National Laboratory, Albuquerque, NM 87185, USA*

Abstract

Large Type-I edge localized modes (ELMs) were completely suppressed by applying edge resonant magnetic perturbations (RMPs) in DIII-D H-mode plasmas with the same low pedestal collisionality ($\nu_e^* \sim 0.1$) as in ITER. The RMP suppressed ELMs by reducing the edge pressure gradient through a reduction in the pedestal density gradient. Divertor emission profiles showed increases in toroidally localized D_α and carbon ion emission and carbon emission throughout both divertor legs. The lowest density ELM-suppressed discharges showed elevated levels of carbon in the core plasma. The data and boundary simulations indicate that the divertor strikepoints make a transition from a high recycling regime during the ELMing phase to a sheath-limited regime during ELM suppression in the lowest density plasmas. ELM suppression during scans of RMP amplitude, injected power and density suggests a possible optimum combination of these actuators for ELM control, without elevated impurity levels, that is extrapolatable to ITER.

PACS: 52.55.Fa; 52.40.Hf; 52.55.Rk; 52.25.Vy; 52.70.Kz

Keywords: DIII-D; ELM; Stochastic boundary; Carbon impurities; Edge plasma

1. Introduction

The transient particle and energy fluxes due to Type-I edge localized modes (ELMs) [1], in standard H-mode operation of ITER [2] are predicted to produce sufficient material erosion to limit the operational lifetime of the divertor plasma facing components (PFCs) to as few as several hundred full power discharges [3,4]. The development of actuators that can reduce the magnitude of these transient fluxes to tolerable levels, while maintaining adequate confinement, is a critical issue for the success of ITER and extrapolation to a power producing tokamak reactor.

* Corresponding author. Fax: +1 858 455 4156.
E-mail address: Fenstermacher@fusion.gat.com (M.E. Fenstermacher).

0022-3115/$ - see front matter © 2007 Elsevier B.V. All rights reserved.
doi:10.1016/j.jnucmat.2007.01.270

The work in this paper focuses on the use of resonant perturbations to the edge magnetic field for control of ELMs in H-mode diverted plasmas. Pioneering work on the effect of edge stochastic fields in circular limited plasmas was done by the Tore-Supra group [5,6 and references therein] and by the TEXTOR group [7–9]. Summaries of work on stochastic magnetic fields in fusion devices can be found in Refs. [10] and [11]. Several other techniques attempting ELM control at high confinement have been pursued previously including pellet ELM pacing by the ASDEX-U group [12], ELM pacing using temporal magnetic triggering by the TCV [13] and ASDEX-U [14] groups, and various small ELM regimes at JT60-U [15], ASDEX-U [16], NSTX [17,18], JET [19], C–Mod [20], JFT-2M [21], and DIII-D [22].

The magnitude of the transient fluxes from ELMs has been controlled in the DIII-D tokamak, in plasmas with the same edge collisionality (ν^*) as predicted for ITER, by application of resonant magnetic perturbations (RMPs) in the edge plasma. This work extends to H-mode confinement and diverted tokamak equilibria, the long history of work, both theoretical and experimental (Refs. [5,6,10,11] and references therein) on the effect of stochastic fields in L-mode circular tokamak plasmas. The work reported here is an extension of DIII-D results reported previously [23–26] which showed that, in high collisionality plasmas, large Type-I ELMs could be replaced by either smaller, Type-II ELMs [22,27] or by rapid edge plasma oscillations, while retaining good H-mode confinement. In the low ν^* plasmas reported here, Type-I ELMs were completely suppressed [28–30] by the RMP from the DIII-D I-coil and no residual transient particle or energy fluxes were observed. Note that the plasma beta in the low ν^* plasmas was substantially higher than in the high ν^* experiments so anticipated effects of beta changes on the interaction of the RMP fields with the axisymmetric field and the non-axisymmetric error fields ([5] and references therein) may also be playing an important role. These experiments are being used to develop sufficient physics understanding of these effects during RMP ELM control to allow confident prediction of its use in future tokamaks.

This paper presents the effects of RMP for ELM control on the pedestal, scrape-off-layer (SOL) and divertor plasmas in DIII-D. A brief description of the experiments is given in Section 2. The detailed effects of RMP application and the resulting ELM suppression on the plasma from the pedestal to the targets at low ν^* are given in Section 3. The results are discussed in Section 4 and conclusions given in Section 5.

2. Brief description of experiments

At low ν^* ELMs were suppressed in low triangularity (δ), lower-single-null (LSN) plasmas held at low density by active cryopumping (Fig. 1). Previous experiments at high ν^* [23–26] showed that the RMP was most effective, in high δ near double-null plasmas, when the edge safety factor (q_{95}) was within a perturbation fields resonance window, $3.5 < q_{95} < 3.9$. For many of the low ν^* experiments the plasma current was increasing, and q_{95} was outside the resonance window at the initial time the RMP was applied. During this period the ELM frequency increased and the amplitude decreased.

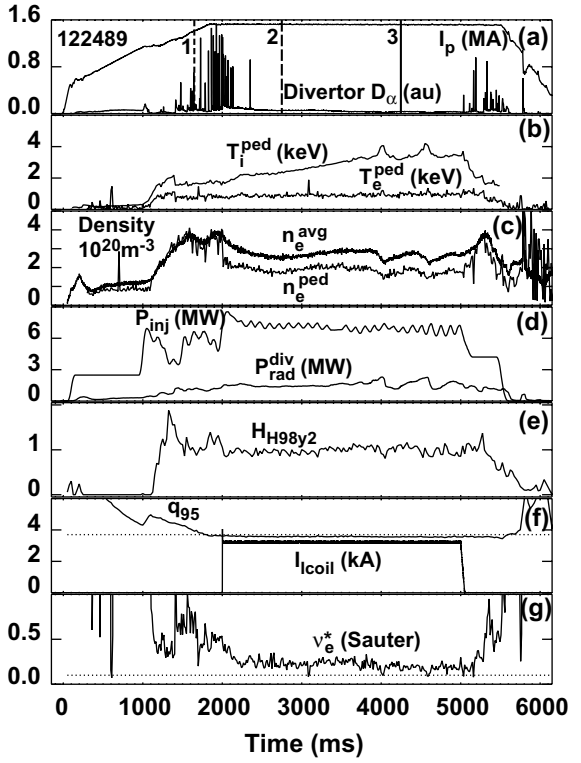

Fig. 1. Low ν^* RMP ELM-suppressed discharge evolution, showing (a) plasma current I_p (MA) and divertor D_α (au), (b) pedestal T_e^{ped} (keV) and T_i^{ped} (keV), (c) line-averaged and pedestal densities (n_e and n_e^{ped} in 10^{20} m^{-3}), (d) injected neutral beam power and divertor radiated power (P_{inj} and P_{rad}^{div} in MW), (e) energy confinement enhancement factor (HH98y2) [2,3], (f) safety factor at 95% flux (q_{95}) and I-coil current I_{Icoil} (kA), and (g) pedestal electron collisionality (ν_e^*) [38].

When q_{95} decreased into the resonance window later in the RMP phase, ELMs were completely suppressed. The core density decreased after ELM suppression but the core temperatures, especially T_i, increased and the total energy content remained nearly constant. At the lowest density the edge collisionality was close to that predicted for ITER, although the edge density was much lower than the ITER value.

Parameter variations showed that ELMs were suppressed when the RMP amplitude was above a threshold value ($\delta B/B_T > 1.8\times10^{-4}$), input beam power was above a threshold ($P_{inj} > 4.2$ MW), and pedestal density was below a threshold ($n_{e,ped} < 2\times10^{19}\,m^{-3}$) [28]. In the scan of RMP amplitude (I-coil current) at fixed power and density, the onset of complete ELM suppression was observed earlier in the discharge [28] for larger RMP amplitude suggesting that the resonance window in q_{95} could be expanded with larger perturbation fields. Divertor gas puffing into ELM-suppressed conditions to increase density showed that complete ELM suppression could be maintained up to a pedestal density of $2.8\times10^{19}\,m^{-3}$. Finally, ELM suppression was more effective as the power and normalized beta ($\beta_N = \beta/(I_p/aB)$) increased [28] up to the maximum power used (10 MW) and maximum $\beta_N = 2.7$.

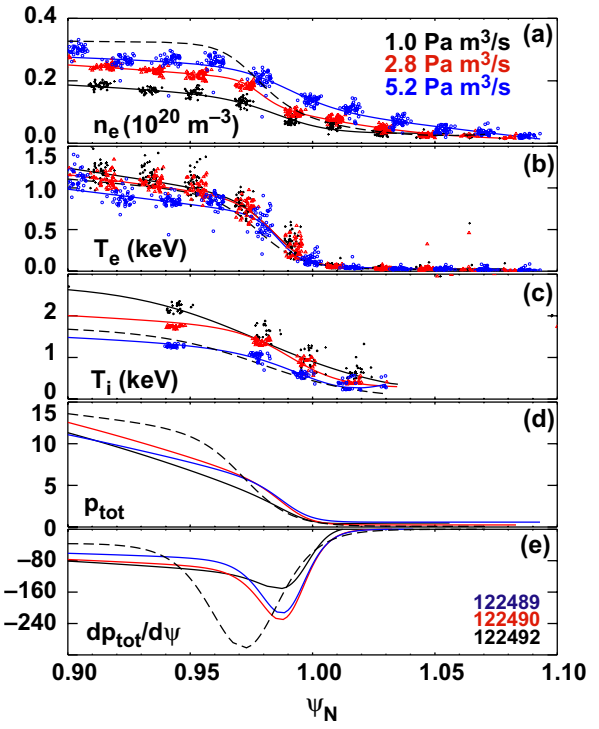

Fig. 2. Profiles from inside the pedestal to the near SOL for (a) n_e (10^{20} m^{-3}), (b) T_e (keV), (c) T_i (keV), (d) total pressure (kPa), and (e) total pressure gradient (kPa/(H/rad)) with same color coding as in Fig. 3. Profiles during ELM suppression are fits to data (n_e and T_e from Thomson scattering and T_i from CER) compiled from 2500 to 3000 ms (Fig. 3). Profiles from the last 20% of the ELM cycle in the pre-RMP ELMing phase (1400–1900 ms) of the low gas rate discharge are shown in dashed-black.

3. Effects of RMP on the pedestal, SOL and divertor

During low ν^*, ELM suppression, the pedestal density n_e^{ped} and density gradient ∇n_e^{ped} are reduced, pedestal electron temperature, T_e^{ped}, and its gradient are increased somewhat, and ion temperature T_i^{ped} increases substantially. This is in contrast to results at high ν^* that showed very little change in the pedestal plasma parameters when the RMP was applied [23–26]. Plasma profiles (Fig. 2) show that n_e^{ped} is reduced (by 40%) and ∇n_e^{ped} is substantially reduced in the ELM-free phase (solid black) compared with profiles just before ELMs (dashed-black). T_e^{ped} increased slightly and ∇T_e^{ped} increased in the barrier region, while T_i^{ped} increased substantially. The profiles shown were obtained from Thomson scattering measurements along a vertical chord above the magnetic axis and approximately 20 cm outboard of the axis. The data were mapped to the outer midplane flux surfaces using an axisymmetric equilibrium so any 3D effects of the RMP fields on islands within the pedestal are not well represented by the mapping. Nevertheless, these profile changes point to a reduction in both the total pressure gradient (up to 55%) (Fig. 3(e)) and the calculated edge bootstrap current due to the ∇n_e^{ped} decrease. Stability analysis assuming axisymmetry [28,29] showed that ELM suppression was achieved by the associated movement of the operating point into a stable region in peeling-ballooning stability space [28,31].

Increasing the gas fueling of RMP ELM-suppressed discharges increased pedestal and core density but it also broadened the far SOL density profile (Fig. 2) and ELMs appeared when n_e^{ped} exceeded a threshold value (Fig. 3). Comparing the n_e^{ped} evolution (Fig. 3(c)) with divertor recycling (Fig. 3(d)–(f)) shows that small rapid ELMs appeared in the intermediate and the high gas rate discharges when n_e^{ped} exceeded a threshold value of $2.8\times10^{19}\,m^{-3}$, for RMP amplitude ($\delta B_r^{(11,3)}/B_T = 2.6\times10^{-4}$, I-coil current = 3 kA) and injected beam power ($P_{inj} = 7.2$ MW). Comparing profiles (Fig. 2)

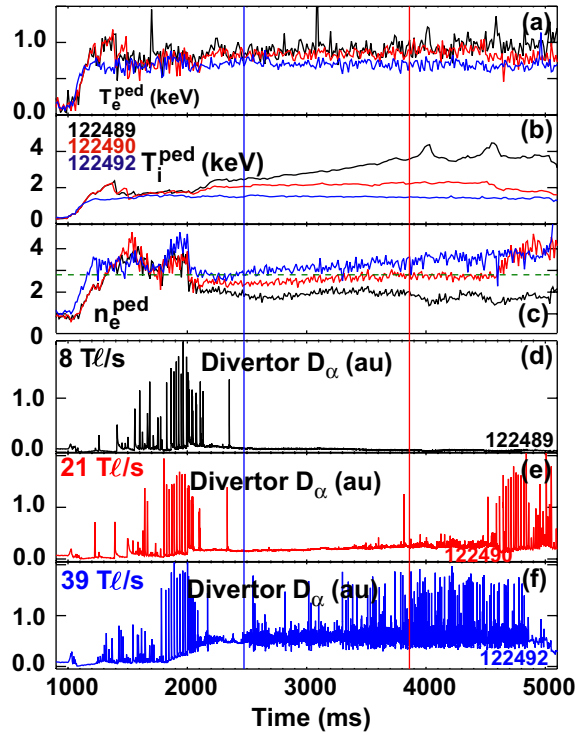

Fig. 3. Evolution of parameters for three gas puffing scan discharges, including (a) pedestal T_e (keV), (b) pedestal T_i (keV), and (c) pedestal n_e (10^{20} m^{-3}). Recycling emission (D_α – au) is given for (d) the low gas puff rate (1.0 Pa m^3/s), (e) the intermediate gas rate (2.8 Pa m^3/s), and (f) the high gas rate (5.2 Pa m^3/s). Vertical lines show times at which small, rapid ELMs appear in the intermediate (red) and high (blue) gas rate discharges.

shows that the intermediate gas rate did increase n_e^{ped} and the total pedestal pressure without inducing ELMs. Higher gas rate did not increase the total pedestal pressure or its gradient further; instead the pedestal produced small, rapid ELMs (Fig. 3(f)). The density profile with the small ELMs shows a much higher SOL density than either of the two profiles without ELMs or the profile just before ELMs from the ELMing phase.

During low v^* ELM suppression, outer midplane measurements showed an increased plasma potential (V_f) near the wall, increased density fluctuations, and decreased magnetic fluctuations from the edge, in contrast to results at high v^* in which the potential did not change much and magnetic fluctuations increased substantially [26]. At low v^*, probe data at the outboard midplane wall showed a large positive (>800 V) floating potential during ELM suppression. Similar high wall potential was seen in low v^*, ELM-free QH-mode plasmas [32]. Analysis of data from multiple density fluctuation diagnostics all showed indications of increased broadband pedestal turbulence, while the density fluctuations level at $\Psi_N = 0.65$ remained constant. Magnetic fluctuations from the plasma boundary associated with ELMs were eliminated at low v^*. In contrast, at high v^* the wall floating potential during ELM suppression remained unchanged at ~0 V and edge magnetic fluctuations increased together with oscillations in D_α and bursts of density fluctuations associated with intermittent transport events.

Divertor conditions changed dramatically when ELMs were completely suppressed at low v^* including substantial increases in carbon emission intensity, localized carbon and deuterium emission near tile edges at divertor strikepoints, and significant changes in heat and particle fluxes to the target plates [33]. Comparing divertor carbon (CIII 465 nm) and deuterium (D_γ 434 nm) emission

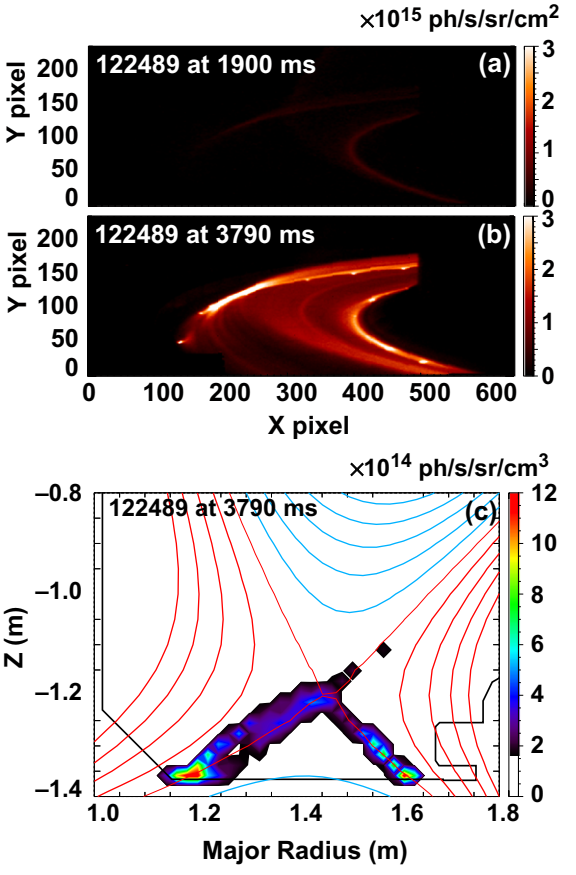

Fig. 4. Tangential view of divertor CIII (465 nm) emission (a) in pre-RMP ELMy H-mode and (b) during RMP ELM suppression, and (c) 2D emission reconstruction during ELM suppression.

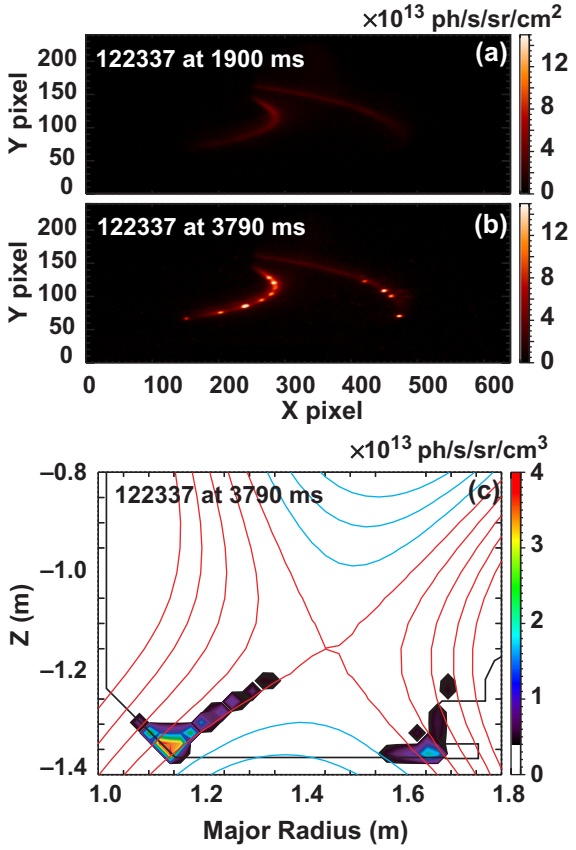

Fig. 5. Tangential view of divertor D_γ (434 nm) emission (a) in pre-RMP ELMy H-mode and (b) during RMP ELM suppression, and (c) 2D emission reconstruction during ELM suppression.

profiles at low density (Figs. 4 and 5) shows the emission averaged over ELMs is nearly toroidally uniform and appears near the inner and outer target strikepoints, but carbon emission increases significantly throughout the divertor during ELM suppression. High intensity CIII emission was seen during ELM suppression at toroidally localized points near gaps between target carbon tiles and the images showed helical striations in both divertor legs that appeared to terminate at the local emission points. The spatial structure of the striations was similar to the geometry of SOL flux tubes. The 2D carbon emission reconstruction during ELM suppression (Fig. 4(c)), albeit smoothing the toroidally distinct striations with an assumption of toroidal symmetry, shows carbon emission all along both divertor legs. Similar increases in toroidal localization of D_γ emission were seen during ELM suppression of a similar low v^* discharge (Fig. 5). The 2D reconstruction shows D_γ emission confined to near the target strikepoints but, when the ELMs are suppressed, strong local emission near the tile gaps is clearly seen (Fig. 5(b)). Finally, outer strikepoint probe data during ELM suppression [33] indicate that the particle flux decreases ($\sim 2x$), target T_e increases ($\sim 2x$), and target V_f is very negative. The steady target heat flux during ELM suppression was approximately the same as that between ELMs in the ELMing phase, but the high ELM heat flux transients were eliminated.

These changes to the pedestal, SOL and divertor conditions can produce a large increase in pedestal and core plasma impurity content during ELM suppression, but the impurity increase is sensitive to the degree of ELM suppression, operating density and the level of edge MHD activity. Z_{eff} profiles associated with C^{6+} ions for two discharges in the density scan are shown in Fig. 6 for times in the pre-RMP ELMing phase, early in the ELM-free phase and

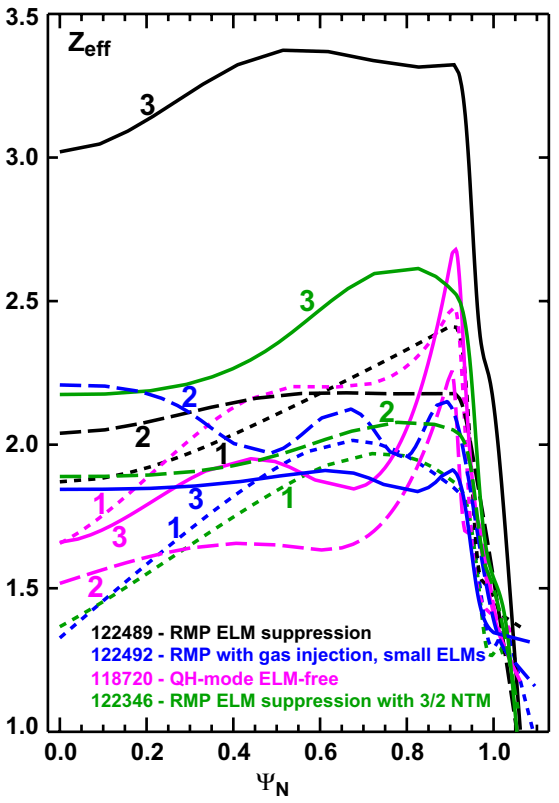

Fig. 6. Profiles of Z_{eff} due to fully ionized C^{6+} for the low v^* baseline discharge from Fig. 1 (black) vs a higher v^* discharge (blue), a comparable v^* QH-mode discharge (magenta) and a comparable v^* discharge with a core MHD mode (green). Profiles at the times indicated by vertical lines in Fig. 1(a) for the low v^* and Fig. 7(a)–(c) for the other discharges respectively.

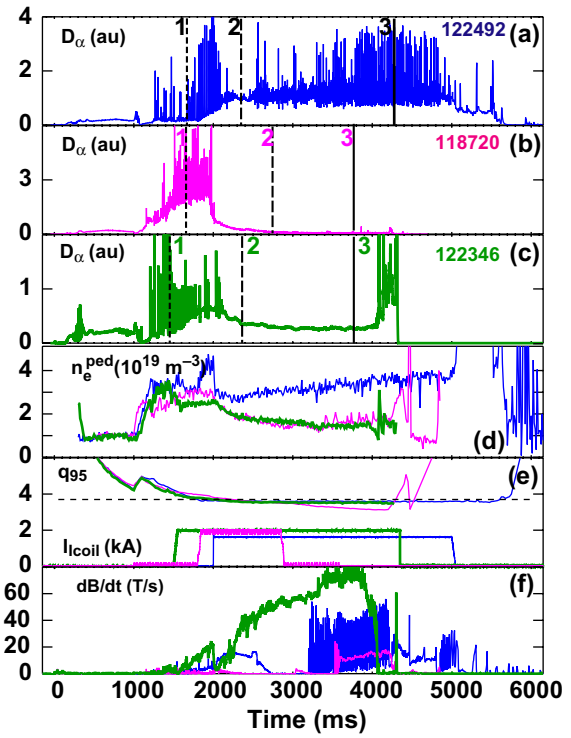

Fig. 7. Evolution of D_α (au) for (a) the higher v^* (blue), (b) QH-mode (magenta) and (c) low density with core MHD (green) discharges. Evolution of (d) n_e^{ped} (10^{20} m^{-3}), (e) q_{95} and I_{Icoil} (kA) and (f) dB/dt (T/s) for all three discharges.

late in the RMP pulse (Fig. 7(a) and (d)–(f)). In both discharges the initial RMP effect early in the ELM suppression was to reduce the pedestal impurity density and increase it near the plasma axis. In the low density discharge, the impurity density across the profile increased with time during ELM suppression resulting in a Z_{eff} increase of $\Delta_{Z_{eff}} = 1.0$ on axis ($\Delta_{Z_{eff}} = 1.2$ in the pedestal). The high-density discharge showed significantly less impurity increase during the RMP phase. In this case, after a 350 ms ELM-suppressed period, small rapid ELMs with a few infrequent large Type-I ELMs began. As the discharge n_e rose due to gas puffing, and the large Type-I ELM frequency increased, impurity density remained essentially constant and Z_{eff} decreased slightly. Similar behavior was seen in the intermediate density discharge; impurity density rose during the ELM-suppressed phase and then began to decrease when small rapid ELMs started.

As an example of low impurity levels in a low density ELM-free plasma, the core Z_{eff} was much lower in an ELM-free QH-mode discharge than in the low density RMP ELM-suppressed case, possibly due to the edge harmonic oscillation (EHO) in the QH-mode discharge. Comparing Z_{eff} profiles (Fig. 6) for a QH-mode discharge (Fig. 7(b) and (d)–(f)) and the low density RMP discharge shows $>2x$ lower impurity density on axis late in the ELM-free period of the QH-mode discharge. The transition to QH-mode and the EHO decreased the impurity density across the entire profile and high levels of impurities were not observed in the core during the QH-mode ELM-free phase.

Even in a low density RMP ELM-suppressed discharge, the impurity density was significantly lower when there was a low level of MHD activity in the core plasma compared with a completely quiet ELM-suppressed discharge (Fig. 6 and Fig. 7(c)–(f)). Here the discharge with lower impurity level had a significant $n = 2$ core MHD mode, the amplitude of which increased with time during ELM suppression. Although Z_{eff} did increase, the increase was less than in the reference RMP discharge.

4. Discussion

Complete suppression of transient particle and energy fluxes from Type-I ELMs, a very positive result for ITER, was achieved in low v^* plasmas in DIII-D, but some of the accompanying effects of the ELM suppression on divertor conditions and core plasma impurity content need further optimization. Many signatures during ELM suppression in the lowest density DIII-D plasmas suggest a sheath-limited divertor regime. This is consistent with high T_e ($\sim 2x$ increase to 90 eV) and large negative floating potential ($\sim 10x$ decrease to -120 V) measured at the target strikepoints [33] and with the observed toroidal localization of carbon and deuterium emission from the targets and increases in core carbon content. This condition arises because the only way to achieve low ITER values of collisionality in DIII-D is to operate at very low density and high power, producing hot divertor plasma at a density that is too low to sustain high recycling near the targets. However, these conditions would likely not be reproduced in low v^* ELM suppression in ITER. First, operation of ITER with RMPs for ELM control would of necessity be accompanied by a divertor target surfaces design optimized to match the expected field structure including the RMP. Second, the high power density in ITER achieves low v^* at much higher plasma density. In fact, for applicability to ITER, RMP ELM suppression would need to be effective

with a partially detached divertor at very high density to keep the steady-state peak heat flux below operating limits.

Modeling of RMP and ELM suppression effects on SOL and divertor conditions confirms that the divertor strikepoints in these low density experiments make a transition from a high recycling regime to a sheath limited regime as the density is reduced and ELMs eliminated. Axisymmetric 2D fluid modeling of the SOL and divertor with UEDGE [34] shows that the plasma very near the strikepoints (within 3 mm mapped to the outer midplane) is in the sheath-limited regime with little density increase or temperature decrease in the poloidal profile approaching the plates. Non-axisymmetric (3D) heat transport simulations in vacuum RMP fields [35] predict much higher transport than seen in the experiments suggesting that the response of the toroidally rotating high β plasma in these experiments is playing an important role in RMP field penetration. Finally, 3D vacuum field line tracing [36,37] predicts that a substantial population of field lines, with short connection length between the pedestal and the targets, would produce radial perturbations of target heat and particle flux profiles with an $n = 3$ toroidal structure.

The goal of ELM control in ITER requires that the physics mechanisms producing complete ELM suppression in low ν^* DIII-D experiments be understood well enough that extrapolation to an optimized ELM control scenario with a combination of RMP amplitude, operating density and power flow through the pedestal, SOL and divertor can be done. The density scan indicates that it should be possible to find a window in DIII-D operating space with small rapid ELMs during RMP application and sufficient density to keep a high recycling condition near the divertor strikepoints. This optimum will require combining higher injected power and RMP amplitude with controlled fuelling to maintain an optimum density, small, rapid ELMs and perhaps a low level of edge MHD activity to help keep impurities out of the core plasma.

5. Conclusions

Impulsive particle and heat loads to divertor targets and main chamber walls from large Type-I ELMs were completely suppressed in DIII-D, while retaining high core energy confinement, by applying steady-state $n = 3$ RMP fields from the DIII-D I-coil at low pedestal collisionalities expected in ITER. Scans of injected power, RMP amplitude and gas fueling rate in ELM-suppressed discharges suggest that it should be possible to demonstrate an optimum ELM control scenario for ITER in future DIII-D experiments through a combination of high injected power, high RMP amplitude and moderate gas fueling. Results indicate that optimum ELM control involves a balance between reduction of impulsive loads to the material surfaces, to reduce sputtering damage, with sufficient edge plasma transport to prevent core plasma penetration of impurities. The experiments reported here provide the existence proof that ELM suppression can be achieved at ITER pedestal collisionalities, but elevated core impurity levels are observed due to loss of the high recycling regime near divertor strikepoints at the extremely low density required to get ITER pedestal collisionalities in DIII-D. Future experiments will extend these results to an optimized scenario of RMP controlled small, rapid ELMs with low core impurity level in an ITER-like high-triangularity shape, with ITER-like low core plasma toroidal rotation.

Acknowledgement

This work was supported by the US Department of Energy under W-7405-ENG-48, DE-FC02-04ER54698, DE-FC02-04ER54758, DE-AC04-94AL85000, and DE-FG03-01ER54615.

References

[1] H. Zohm et al., Plasma Phys. Control. Fus. 38 (1996) 105.
[2] ITER Physics Basis Document 1999 Nucl. Fus. (39) 2137, Tokamak Physics Basis, Nucl. Fus. in press.
[3] G. Federici et al., J. Nucl. Mater. 313–316 (2003) 11.
[4] A.W. Leonard et al., J. Nucl. Mater. 313–316 (2003) 768.
[5] Ph. Ghendrih et al., Plasma Phys. Control. Fus. 38 (1996) 1653.
[6] Ph. Ghendrih et al., Nucl. Fus. 42 (2002) 1221.
[7] K.H. Finken et al., J. Nucl. Mater. 220–222 (1995) 448.
[8] K.H. Finken et al., Plasma Phys. Control. Fus. 46 (2004) B143.
[9] R.C. Wolf et al., Nucl. Fus. 45 (2005) 1700.
[10] K.H. Finken, Ed. Nucl. Fus. 44 (2004) S1.
[11] K.H. Finken, Ed. Nucl. Fus. 46 (2006) S107.
[12] P.T. Lang et al., Nucl. Fus. 44 (2004) 665.
[13] A.W. Degeling et al., Plasma Phys. Control. Fus. 45 (2003) 1637.
[14] P.T. Lang et al., Plasma Phys. Control. Fus. 46 (2004) L31.
[15] Y. Kamada et al., Plasma Phys. Control. Fus. 38 (1996) 1387.
[16] J. Stober et al., Plasma Phys. Control. Fus. 42 (2000) A211.
[17] R. Maingi et al., Nucl. Fus. 45 (2005) 264.

[18] R. Maingi et al., Nucl. Fus. 45 (2005) 1066.
[19] G. Saibene et al., Nucl. Fus. 45 (2005) 297.
[20] Y. Takase et al., Phys. Plasmas 4 (1997) 1647.
[21] K. Kamiya et al., Nucl. Fus. 43 (2003) 1214.
[22] T. Ozeki et al., Nucl. Fus. 30 (1990) 1425.
[23] T.E. Evans et al., Phys. Rev. Lett. 92 (2004) 235003-1.
[24] T.E. Evans, J. Nucl. Mater. 337–339 (2005) 691.
[25] T.E. Evans et al., Nucl. Fus. 45 (2005) 595.
[26] R.A. Moyer et al., Phys. Plasmas 12 (2005) 056119.
[27] T.H. Osborne, et al., in: Proceedings of 32nd EPS Conference on Controlled Fusion and Plasma Physics, Tarragona, Spain 2005, vol. 29C, European Physical Society, 2005, Paper P-4.012.
[28] K.H. Burrell et al., Plasma Phys. Control. Fus. 47 (2005) B37.
[29] T.E. Evans et al., Phys. Plasmas 13 (2006) 056121.
[30] T.E. Evans et al., Nature Phys. 2 (2006) 419.
[31] P.B. Snyder et al., Phys. Plasmas 12 (2005) 056115; P.B. Snyder et al., Phys. Plasmas 9 (2002) 2037; P.B. Snyder et al., Nucl. Fus. 44 (2004) 320.
[32] K.H. Burrell et al., Phys. Plasmas 12 (2005) 056121.
[33] J.G. Watkins, et al., J. Nucl. Mater., these Proceedings, doi:10.1016/j.jnucmat.2007.01.064.
[34] T.D. Rognlien et al., J. Nucl. Mater. 196–198 (1992) 347.
[35] I. Joseph et al., J. Nucl. Mater., these Proceedings, doi:10.1016/j.jnucmat.2006.12.067.
[36] T.E. Evans et al., J. Nucl. Mater., these Proceedings, doi:10.1016/j.jnucmat.2006.12.064.
[37] L.W. Yan et al., J. Nucl. Mater., these Proceedings, doi:10.1016/j.jnucmat.2007.01.192.
[38] O. Sauter et al., Phys. Plasmas 6 (1999) 2834.